NASA Technical Paper 2055

October 1982

Materials Constitutive Models for Nonlinear Analysis of Thermally Cycled Structures

Albert Kaufman
and Larry E. Hunt

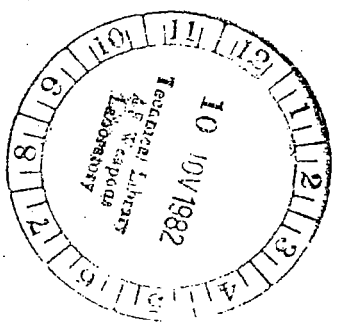

NASA

NASA
Technical
Paper
2055

1982

Materials Constitutive Models for Nonlinear Analysis of Thermally Cycled Structures

Albert Kaufman
Lewis Research Center
Cleveland, Ohio

Larry E. Hunt
University of Arizona
Tucson, Arizona

National Aeronautics
and Space Administration

**Scientific and Technical
Information Branch**

effects on calculated hysteretic response of different inelastic constitutive models available in nonlinear analysis computer codes. The hysteretic response is required for component life prediction.

The structural analyses were performed on an IN 100 alloy double-edge wedge specimen that was thermally cycled in fluidized beds maintained at 316° and 1088° C with an immersion time of 3 minutes in each bed. The specimen geometry was modeled with 20-node, isoparametric, three-dimensional elements. Nonlinear analyses were performed by using isotropic, kinematic, and combined isotropic-kinematic hardening models and a combined hardening model in conjunction with a strain-hardening creep law to account for cyclic time-dependent effects. Monotonic stress-strain properties were used for the isotropic and combined models, and saturated cyclic stress-strain properties were used for the kinematic model. An elastic analysis was also performed as a baseline case. The results from the different constitutive models and the elastic analysis were compared with respect to (1) predicted hysteretic behavior, (2) computational efficiency, (3) input data requirements, and (4) ease of use.

Analytical Procedure

Stresses, total strains, and inelastic strains were calculated for a double-edge wedge specimen of IN 100 alloy that was thermally cycled in fluidized beds maintained at 316° and 1088° C with an immersion time of 3 minutes in each bed. The analytical conditions and methods are discussed in this section.

Input for Analyses

The specimen geometry, material properties, and thermal loading that were used as input to the structural analyses are described here.

Geometry. – The geometry of the double-edge wedge specimen is illustrated in figure 1. To be consistent with the structural analyses of references 9 and 12, the leading-edge and trailing-edge radii were squared off to 1.02- and 1.53-millimeter lengths, respectively, for the finite-element model. Otherwise the finite-element model duplicated the geometry exactly.

Material properties. – The physical properties of the IN 100 alloy are presented in table I. Mean thermal coefficient of expansion data were obtained from reference 9; these values were converted to instantaneous coefficients of thermal expansion for input into the MARC program. The modulus of elasticity was determined from monotonic stress-strain tests of tensile specimens. Cyclic stress-strain curves were obtained by using the single-specimen incremental step procedure and equipment described in reference 19. A typical cyclic

TABLE I. - IN 100 ALLOY PHYSICAL PROPERTIES

Temperature, °C	Modulus of elasticity, MN/m^2	Mean coefficient of thermal expansion, m/m/°C
316	193×10^3	13.1×10^{-6}
371	190	13.3
427	186	13.5
482	183	13.7
538	179	13.9
593	176	14.0
649	172	14.4
704	168	14.6
760	163	14.9
816	157	15.4
871	152	15.8
927	145	16.4
982	139	16.7
1038	133	17.5
1093	127	18.2

stress-strain curve, with the loci of the curve tips represented by an exponential equation, is illustrated in figure 2. Also shown for comparison in figure 2 is a monotonic stress-strain curve represented by an exponential equation. Short-time cyclic creep tests were conducted on IN 100 specimens by using the procedures and facilities described in reference 20. Preprocessor programs expressed both the cyclic stress-strain and creep data as functional relations in exponential form. These equations were incorporated into MARC by means of user subroutines. The constants of the cyclic and monotonic stress-strain equations are given in table II for various temperatures. The constants of the cyclic creep equations are given in table III for various temperatures. The negative exponent on the stress term at 649° C in table III is due to extrapolation of the creep equation below the temperature range of the data (800° to 1100° C); this is not considered a significant anomaly because of the low creep rate at this temperature.

Thermal loading. – The transient temperature loading on the double-edge wedges was determined from thermocouple data. The location of the thermocouples at the wedge cross section is shown in figure 3. The thermocouple outputs were cross plotted to give temperatures of the midchord at the midspan at various time increments after immersion into the fluidized beds; these data are presented in figure 3. It was assumed that there was no temperature gradient through the thickness of the wedge. Another set of thermocouple data were taken with five thermocouples mounted along the leading edge over half the span. These data revealed a longitudinal (along the span of the specimen) temperature gradient that varied with the different time

TABLE II. - IN 100 ALLOY STRESS-STRAIN PROPERTIES

Temperature, °C	Cyclic,[a,b] $\sigma = K(10\ \epsilon_p)^n$		Monotonic,[b,c] $\sigma = C(10\ \epsilon_p)^m$	
	K	n	C	m
316	1005	0.046	731	0.078
427	944	.064	↓	↓
538	869	.086		
649	777	.113		
760	665	.147		
871	528	.187	676	
982	361	.236	255	.146
1093	157	.297	173	.146

[a]Locus of cyclic curve tips (fig. 2).
[b]Stress σ in megapascals; plastic strain ϵ_p in percent.
[c]Not applicable for ϵ_p less than 0.02 percent.

TABLE III. - IN 100 ALLOY CREEP PROPERTIES

Temperature, °C	Creep rate,[a] $\dot{\epsilon}_{cr} = A(\sigma/6.895)^m(t)^n$, percent/min		
	A	m	n
649	0.00161	-0.806	-1.088
760	.00062	.717	-.881
871	.00012	1.709	-.736
982	.00010	2.172	-.654
1093	.00058	2.103	-.634

[a]Stress σ in megapascals; time t in minutes.

increments. A least-squares best fit parabola was determined for each time increment and is presented in table IV. This parabolic temperature variation along the span was assumed over the complete chord of the wedge. Details of the installation and procedure are given in reference 7.

The temperatures at the midspan were determined from the appropriate plot in figure 3. For locations other than midspan the temperatures were determined by using the midspan temperature modified by the values given in table IV. Therefore by using figure 3 and table IV the temperature distribution at any point of the wedge was determined.

A preprocessor program converted the thermal loading data from the wedge specimen into the form of sixth-order polynomial equations. A subroutine that was inserted into MARC interpolated from these equations for the local temperatures at the Gaussian integration points of the finite-element model.

Methods of Analysis

Stress and total-plastic-creep strain distributions in the wedge specimens were calculated from the MARC nonlinear, finite-element computer program. Computations were performed for 34 time increments (17 heating, 17 cooling) into which the thermal cycle was subdivided, as shown in figure 3. The analyses were continued until reasonably stable stress-strain hysteresis loops were obtained or, if still unstable, were terminated after three cycles of analysis.

Plasticity computations were based on incremental plasticity theory using the von Mises yield criterion and normality flow rule. The yield surface under reversed loading was determined from the stress-strain properties and the selected hardening model. Three hardening models available in MARC (isotropic, kinematic, and combined isotropic-kinematic) were selected for evaluation. Monotonic stress-strain properties were used in conjunction with the isotropic and combined models because of their initial instability. Saturated cyclic stress-strain properties were used for the stable kinematic model. A bilinear representation of the cyclic stress-strain curve, as shown in figure 2, was applied to the kinematic hardening model. The slope of the kinematic model was determined from energy considerations so that the strain energy, as indicated by the enclosed area, would be identical with that of the actual cyclic stress-strain curve. Creep effects during the cycle were considered for one case involving the combined model by imposing four 30-second hold times during heating and two 6-second hold times at the start of the cooling part of the cycle. These intervals were selected because the combination of temperatures and stresses indicated a possibility of the occurrence of significant creep at these times in the thermal transient. The creep computations utilized the cyclic creep data in conjunction with a strain-hardening rule. A subroutine that was inserted into the MARC program in the form of yield strengths and work-hardening slopes as functions of temperature was used to determine the stress-strain properties for the local temperatures at the Gaussian integration points. Similarly the creep properties and laws were coded into another user subroutine that was used to obtain the creep strains at the integration points.

Outputs from the program were the effective, normal, and shear stresses, the equivalent total and plastic strains, the normal and shear total and plastic strains, and the nodal displacements. Stress and strain output were given

TABLE IV. - TEMPERATURE VARIATION ALONG SPAN

[$T_{x,z} = T_{x,ms}(Az^2 + Bz + C)$, where $T_{x,z}$ is the temperature at any x,z coordinate (see fig. 4), $T_{x,ms}$ is the temperature at the x coordinate at midspan, and z is the span coordinate; all temperatures in °F ($F = 9/5\ C + 32$) and all x and z coordinates in inches.]

Time increment, sec	Heating bed			Cooling bed		
	A	B	C	A	B	C
0	-0.00870	0.0517	0.9205	-0.00666	0.03957	0.9427
3	.04401	-.2614	1.3891	-.01775	.1055	.8447
6	.03739	-.2221	1.3290	-.02384	.1416	.7911
9	.03688	-.2191	1.3372	-.02548	.1514	.7786
12	.03806	-.2261	1.3344	-.02731	.1622	.7622
15	.03695	-.2195	1.3300	-.02889	.1716	.7480
30	.02758	-.1638	1.2504	-.03047	.1810	.7338
45	.01769	-.1051	1.1630	-.03141	.1866	.7224
60	.01432	-.08506	1.1324	-.03442	.2044	.6905
75	.01006	-.05978	1.0934	-.03265	.1939	.7093
90	.00803	-.04948	1.0791	-.02867	.1703	.7440
105	.00557	-.03311	1.0528	-.02445	.1452	.7843
120	.00627	-.03722	1.0571	-.02276	.1352	.7981
135	.00440	-.02614	1.0415	-.01876	.1142	.8323
150	.00371	-.02205	1.0357	-.01533	.09107	.8622
165	.00297	-.01762	1.0285	-.01278	.07593	.8832
180	.00262	-.01553	1.0243	-.01212	.07198	.8876

for the Gaussian integration points. To prevent excessive generation of computer printout, the output was restricted to high-strain regions of the model. Contour plots of effective stress, longitudinal stress and total strain, equivalent total, plastic, and creep strain, and temperature were obtained at the time increments of maximum and minimum total strain in the cycle.

Finite-Element Model

The finite-element model is illustrated in figure 4. Because of symmetry only one-fourth of the wedge specimen needed to be modeled; this model was bounded by the surface and intersecting midchord and midspan planes of symmetry. The element used was a 20-node, isoparametric, three-dimensional block with 8 corner nodes and 12 edge midpoint nodes. This element had 27 Gaussian integration points. The model consisted of 36 of these elements with a total of 315 nodes and 778 unsuppressed degrees of freedom.

All nodes initially on the midspan and midchord faces of the model were constrained to lie on the midspan and midchord planes, respectively. In addition, one node at the leading edge was constrained chordwise (leading to trailing edge) in order to prevent rigid-body motion in that direction.

Results and Discussion

The results of the MARC nonlinear and elastic analyses of a thermally cycled double-edge wedge specimen of IN 100 alloy are discussed herein. Analytical results are presented for each inelastic constitutive model (combined, combined with creep, isotropic, and kinematic) and from the elastic analysis. Comparisons are made among these different stress-strain behavior relations. The discussion is based primarily on the analytical results at the location in the specimen where the maximum total strain range was computed during the cycle. This location (henceforth, called the critical location) occurred in all the analytical cases at the leading edge at a quarter of the specimen span from either end; this location is in agreement with experimental crack initiation data for the wedge specimens that are reported in reference 21. The stress-strain results discussed below for the critical location were actually computed at the closest Gaussian integration point, which was 0.056 centimeter from the surface at the quarter span.

Evaluation of Models

The metal temperature cycle is presented in figure 5. The temperature at the critical location varied from

343° C at the start of the cycle to 1077° C at the end of the heating immersion. This temperature spectrum applied to all of the elastic and nonlinear analysis cycles since the critical location did not change. The stress-strain solutions at the critical location from the MARC elastic and nonlinear analyses are summarized in figures 6 to 9 as functions of the load-time increments. All stresses and strains in these figures were effective or equivalent values that were computed as positive numbers. However, in order to later construct stress-strain hysteresis loops, the stresses and total strains were assigned positive or negative signs depending on the signs of the highest magnitude principal stresses or strains.

Elastic. – Figures 6(a) and (b) show the variations in stress and total strain, respectively. Stresses and strains were compressive during the heating part of the cycle, with the minimum values occurring after 30 seconds of heating (increment 7). The stresses and strains were tensile during cooling, with the maximum values occurring after 9 seconds of cooling (increment 21).

Combined. – Figure 7 shows the results from the nonlinear analysis using the combined isotropic-kinematic hardening model. This analysis was terminated before completion of the second cycle when it became apparent that the stress-strain state had stabilized. Stabilization is demonstrated in figure 7(c), where it is shown that all of the plastic straining took place during the first 60 seconds of heating (increments 1 to 9) and that there was no further plastic flow thereafter. As in the elastic analysis the total strains, but not stresses, were minimum after 30 seconds of heating (increments 7 and 41) and maximum after 9 seconds of cooling (increments 21 and 55).

Combined-creep. – Figure 8 shows the results of the nonlinear analysis using the combined model with creep. The analysis was terminated during the third cycle because of computer problems. Figures 8(c) and (d) illustrate the destabilization of the problem by interposing creep hold times at discrete intervals in the thermal transients. The equivalent plastic strains decreased (fig. 8(c)) while the equivalent creep strains increased (fig. 8(d)) although at diminished rates during cycling. Only slight changes in the maximum creep strains were obtained with further cycling. In absolute terms the plastic and creep strains were always compressive during the thermal cycling; therefore the maximum equivalent creep strains in figure 8(d) were actually minimum absolute values and the minimum equivalent creep strains were maximum absolute values. Since the automatic creep option in MARC creates additional increments during creep hold times, the increment numbers in figure 8 are not comparable to those in figures 5 to 7 and 9. The total strains (fig. 8(b)) reached their minimum values at the end of the creep hold time for 30 seconds of heating (increments 19, 107, and 193) and their maximum values at the beginning of the hold time for 9 seconds of cooling (increments 71 and 157).

Isotropic. – The isotropic hardening model gave essentially the same stress-strain solutions as were obtained with the combined model without creep. This similarity in results was due to the use of the same monotonic stress-strain properties and the absence of plastic strain reversal during cycling. Therefore the discussion of results for the combined model without creep is also applicable to isotropic hardening, and the latter will not be discussed separately.

Kinematic. – The results of the nonlinear analysis using the kinematic hardening model are given in figure 9. These results show that an unstable stress-strain state still existed after three analytical cycles. This instability is most clearly shown in figure 9(c), where the maximum and minimum equivalent plastic strains for each cycle decrease as the cycling proceeds (or increase in an absolute sense since the plastic strains were predominantly compressive). As in the elastic and other nonlinear analyses, the minimum total strains occurred after 30 seconds of heating (increments 7, 41, and 75) and the maximum total strains occurred after 9 seconds of cooling (increments 21, 55, and 89). The differences in the stress-strain states between cycles were relatively minor in terms of stress (fig. 9(a)) and total strain (fig. 9(b)) as compared with the plastic strain changes shown in figure 9(c)).

Comparison of Models

Comparisons are made in figures 10 to 13 of the stress-strain solutions for the second cycle from the nonlinear analyses for each constitutive model. The elastic analysis results are also presented in these comparisons as a baseline case.

In figure 10 the stress-strain hysteresis loops for each of the nonlinear analyses are compared with the elastic response. The stresses and total strains in figure 10 were, as discussed previously, effective or equivalent values that were assigned signs on the basis of whether the principal stresses or strains were predominantly tensile or compressive. These results suggest that the total strain range was not appreciably affected by the choice of constitutive model or the type of stress-strain data and that an elastic analysis was adequate for the computation of the total strain range. The major differences between the elastic and nonlinear hysteresis loops were in the stress levels, which shifted in the tensile direction under inelastic straining, and the enclosed areas within the loops. A measure of the strain energy or inelastic work is the area of the hysteresis loop. The widest hysteresis loop, and therefore the most inelastic work, is shown by the kinematic hardening model in figure 10(d); the next widest, by the combined-creep model in figure 10(c).

Since there was no further plastic straining during the second cycle when using the combined hardening model without creep, there was no inelastic work, and as expected the areas of the nonlinear and elastic hysteresis loops shown in figure 10(a) were approximately the same.

Some of the second-cycle parameters are compared for the four analyses in figure 11. Significant differences in the mean stresses of the elastic and nonlinear hysteresis loops are apparent in figure 11(a). The greatest stress shift was exhibited by the combined hardening model; the introduction of creep hold times during the thermal transients had only a slight effect on the mean stress under combined hardening. Figure 11(b) confirms the previous observation based on the hysteresis loops of figure 10 that the computed total strain range was essentially constant for all of the analyses; even the largest total strain range (kinematic) was only 5 percent greater than the smallest (combined-creep). The selection of constitutive model had a major effect on the computed inelastic strain range (fig. 11(c)). The greatest plastic strain change was exhibited by the kinematic model, while the combined model without creep showed no change during the second cycle. The inclusion of creep effects with the combined model caused creep strain ratchetting and a relatively smaller change in plastic strain; the net inelastic strain change would be the difference of these since the equivalent plastic strains decreased in figure 8(c) and the equivalent creep strains increased in figure 8(d) with the number of cycles. Figure 11(d) compares the inelastic work done during the second cycle; the work was calculated by summing the product of the effective stress and the incremental equivalent inelastic strain at the critical location for each increment. The kinematic model showed about two and one-half times the amount of work as was done with the combined-creep model. No plastic work was performed with the combined model without creep since there was no plastic flow during the second cycle.

One of the most important considerations in deciding whether to perform a nonlinear analysis or how many cycles to continue it is the computing time. Figure 11(e) summarizes the computing time required per cycle for each of the analyses. As expected, the elastic analysis was the most rapid because the constant reassembly and solution of the stiffness matrix could be avoided during incremental loading; also the elastic analysis only had to be performed for one cycle. The nonlinear analyses using the combined and kinematic hardening models required 40 to 45 minutes of computing time per cycle on the IBM 370 system as compared with 8 minutes for the elastic analysis. The addition of creep hold times amounting to about 37 percent of the total cycle time increased the computing time by 50 percent.

Temperature, stress, and strain distributions along the midchord plane are presented in figure 12 after 30 seconds of heating and in figure 13 after 9 seconds of cooling when the total strains were minimum and maximum, respectively. The highest temperatures during heating (fig. 12(a)) and the lowest temperatures during cooling (fig. 13(a)) were reached at the leading edge. This temperature distribution resulted in the leading edge having the highest longitudinal compressive stresses during heating (fig. 12(c)) and the highest longitudinal tensile stresses during cooling (fig. 13(c)). In figures 12(d) and 13(d) the largest equivalent total strains are shown on the leading edge at about the center of the finite-element model (quarter span), where the critical location was determined. The maximum equivalent plastic strains were also at the leading edge but somewhat below quarter span, as shown in figures 12(e) and 13(e). However, the creep strains from the combined-creep model analysis were as large or larger on the trailing edge.

Of the nonlinear models considered in this study, the isotropic model and the combined model without creep were the easiest to use and required the least inelastic material property data. Interposing creep hold times during the thermal transients made the analysis difficult to perform because it involved constant switching between plastic and creep computations, caused bookkeeping problems, and required periodic reprogramming of user subroutines to account for the creep increments. The results of this study indicate that, except for total strain range, structural parameters used in low-cycle-fatigue damage models such as mean stress, inelastic strain range, and inelastic work are sensitive to the constitutive model used in the nonlinear analysis.

Summary of Results

Three-dimensional finite-element analyses were performed on a thermally cycled, double-edge wedge specimen of IN 100 alloy in order to evaluate different inelastic constitutive models available in the MARC nonlinear, structural computer program. The major results of this study were as follows:

1. Of the structural analysis parameters used in low-cycle-fatigue damage models only the total strain range was relatively insensitive to the choice of inelastic constitutive model. Other parameters such as inelastic strain range, mean stress, and inelastic work were significantly affected by the constitutive model.

2. Elastic analysis was adequate for the calculation of the maximum total strain range. The elastic analysis was also able to determine the critical location for crack initiation and the cycle times when the total strain was maximum or minimum. Maximum total strain ranges computed from the elastic and nonlinear analyses agreed within 5 percent.

3. The use of the isotropic and combined isotropic-kinematic hardening models without creep resulted in stable stress-strain hysteresis loops after the first cycle. The similarity in results with these two models was due to the use of the same stress-strain properties and the absence of plastic strain reversal. Creep analysis in conjunction with the combined model destabilized the hysteretic behavior and caused creep ratchetting and relatively small plastic straining on succeeding cycles.

4. The largest inelastic strain range and most inelastic work per cycle occurred with the kinematic hardening model. The combined model showed no inelastic work after initial heating on the first cycle.

5. Inelastic straining caused the stress-strain hysteresis loops to shift in the tensile stress direction. Mean stress levels varied considerably with the constitutive model used in the nonlinear analysis. The greatest stress shift was exhibited by the combined hardening model. Creep effects had only a slight influence on the mean stress.

6. The elastic-plastic analyses used about five or six times the computing time per cycle that was required by the elastic analysis. Also the elastic analysis only had to be performed for one cycle. Inclusion of creep effects in the nonlinear analysis substantially increased the computing time, as well as the difficulty in performing the analysis, because of the constant switching between plasticity and creep computations.

7. Of the nonlinear analysis methods considered in this study, the isotropic and combined hardening models without creep were the easiest to use and required the least inelastic material property data.

Lewis Research Center
National Aeronautics and Space Administration
Cleveland, Ohio, April 5, 1982

References

1. Hirschberg, M. H.; and Halford, G. R.: Use of Strainrange Partitioning to Predict High-Temperature Low-Cycle Fatigue Life. NASA TN D-8072, 1976.
2. Saltsman, J. F.; and Halford, G. R.: Application of Strainrange Partitioning to the Prediction of Creep-Fatigue Lives of AISI Types 304 and 316 Stainless Steel. J. Pressure Vessel Technol., vol. 99, no. 2, May 1977, pp. 264–271.
3. Hirschberg, M. H.; and Halford, G. R.: Strainrange Partitioning – A Tool for Characterizing High-Temperature Low-Cycle Fatigue. NASA TM X-71691, 1975.
4. Halford, G. R.; Saltsman, J. F.; and Hirschberg, M. H.: Ductility Normalized-Strainrange Partitioning Life Relations for Creep-Fatigue Life Prediction. Proceedings of the Conf. on Environmental Degradation of Engineering Materials, M. R. Louthan, Jr., and R. P. McNih, eds., Virginia Tech. Printing Dept., 1977, pp. 599–612.
5. Manson, S. S.; Halford, G. R.; and Hirschberg, M. H.: Creep Fatigue Analysis by Strain-Range Partitioning. Design for Elevated Temperature Environment, S. Y. Zamrik, ed., ASME, 1971, pp. 12–24.
6. Spera, D. A.; and Grisaffe, S. J.: Life Prediction of Turbine Components: On-Going Studies at the NASA Lewis Research Center. NASA TM X-2664, 1973.
7. Bizon, P. T.; and Spera, D. A.: Comparative Thermal Fatigue Resistances of Twenty-Six Nickel- and Cobalt-Base Alloys. NASA TN D-8071, 1975.
8. Bizon, P. T.; et al.: Three Dimensional Finite-Element Elastic Analysis of a Thermally Cycled Single-Edge Wedge Geometry Specimen. NASA TM-79026, 1979.
9. Drake, S. K.; et al.: Three-Dimensional Finite-Element Elastic Analysis of a Thermally Cycled Double-Edge Wedge Geometry Specimen. Nickel Alloy Turbine Parts. AFWAL-TR-80-2013, Air Force Wright Aeronautical Labs., 1980. (AD-A083245.)
10. MARC General Purpose Finite Element Analysis Program. User Manual. Vols. A & B, MARC Analysis Research Corp., 1979.
11. Kaufman A.: Elastic-Plastic Finite-Element Analyses of Thermally Cycled Single-Edge Wedge Specimens. NASA TP-1982, 1982.
12. Kaufman A.: and Hunt, L. E.: Elastic-Plastic Finite-Element Analyses of Thermally Cycled Double-Edge Wedge Specimens. NASA TP-1973, 1982.
13. Kaufman, A.; and Gaugler, R. E.: Cyclic Structural Analyses of Air-Cooled Gas Turbine Blades and Vanes. SAE Trans., vol. 85, Sept. 1976.
14. Kaufman, A.; and Gaugler, R. E.: Nonlinear, Three-Dimensional Finite-Element Analysis of Air-Cooled Gas Turbine Blades. NASA TP-1669, 1980.
15. Kaufman, A.: Comparison of Elastic and Elastic-Plastic Structural Analyses for Cooled Turbine Blade Airfoils. NASA TP-1679, 1980.
16. Moreno, V.: Combustor Liner Durability Analysis. (PWA 5684-19, Pratt & Whitney Aircraft Group.) NASA CR-165250, 1981.
17. McKnight, R. L.; Laflen, J. H.; and Spamer, G. T.: Turbine Blade Tip Durability Analysis. (R81AEG372, General Electric Co.) NASA CR-165268, 1981.
18. Armen, H.: Assumptions, Models, and Computational Methods for Plasticity. Comput. Struct., vol. 10, no. 1-2, April 1979, pp. 161-174.
19. Nachtigall, A. J.: Cyclic Stress-Strain Curve Determination for D6AC Steel by Three Methods. NASA TM-73815, 1977.
20. Halford, G. R.: Cyclic Creep-Rupture Behavior of Three High-Temperature Alloys. Metall. Trans., vol. 3, no. 8, Aug. 1972.
21. Howes, M. A. H.: Thermal Fatigue Data on 15 Nickel- and Cobalt-Base Alloys. (IITRI-B6078-38, IIT Research Institute.) NASA CR-72738, 1970.

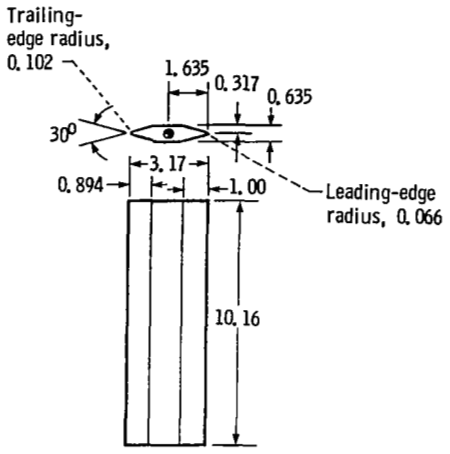

Figure 1. - Double-edge wedge. (All linear dimensions in centimeters.)

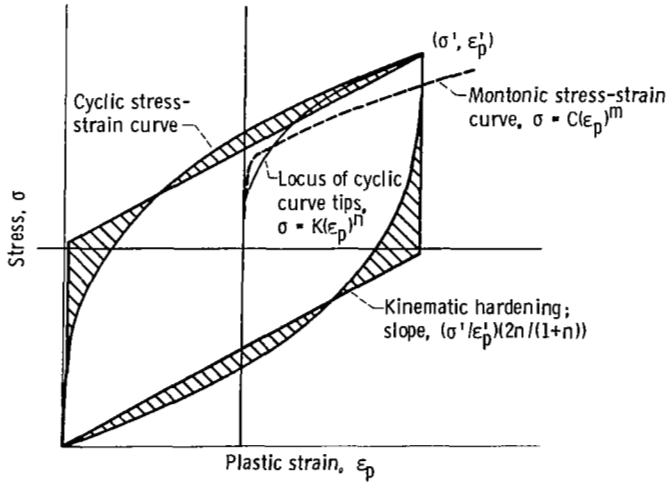

Figure 2. - Representation of stress-strain curves.

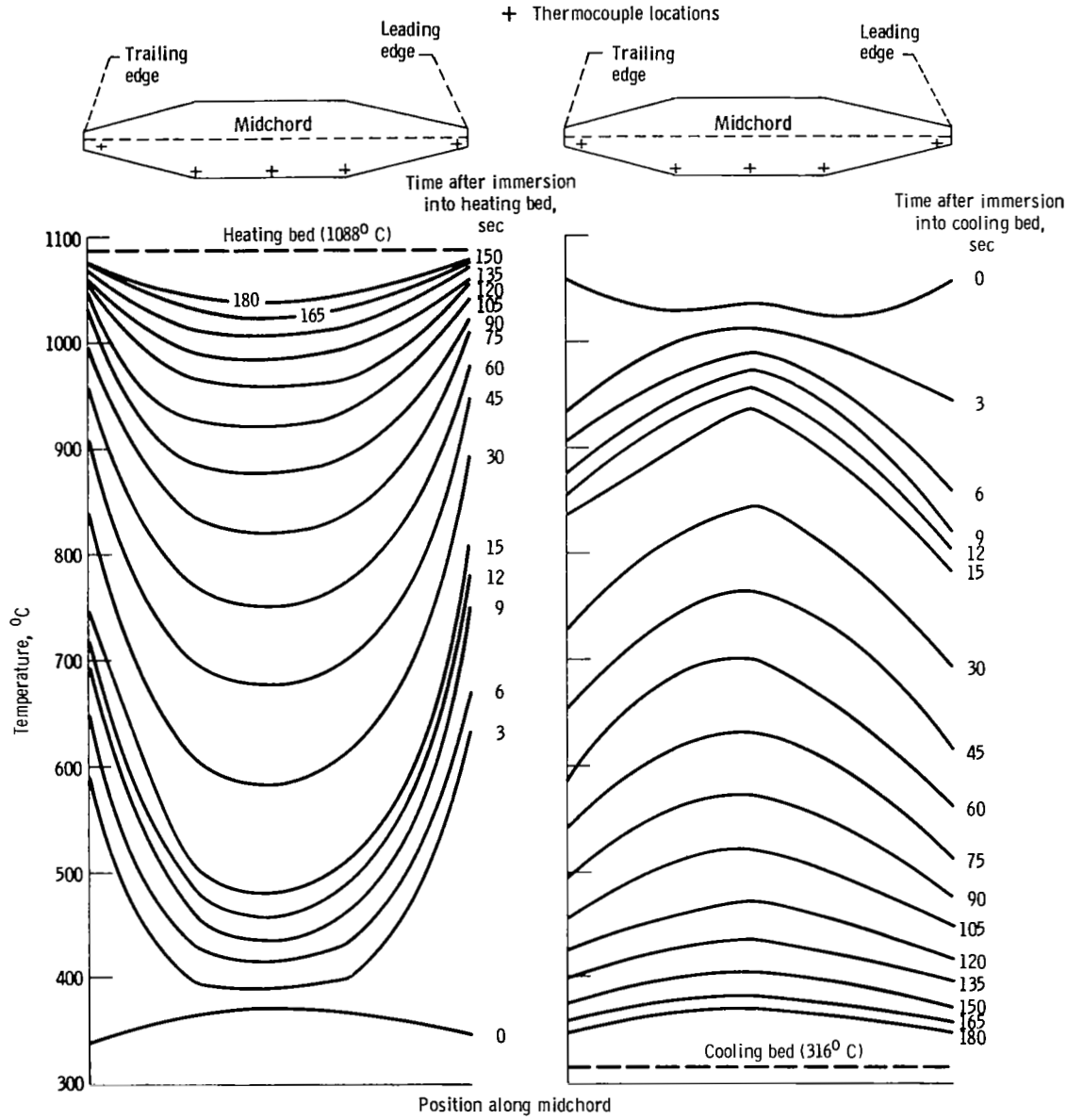

Figure 3. - Temperature at midspan at various times after immersion into fluidized beds.

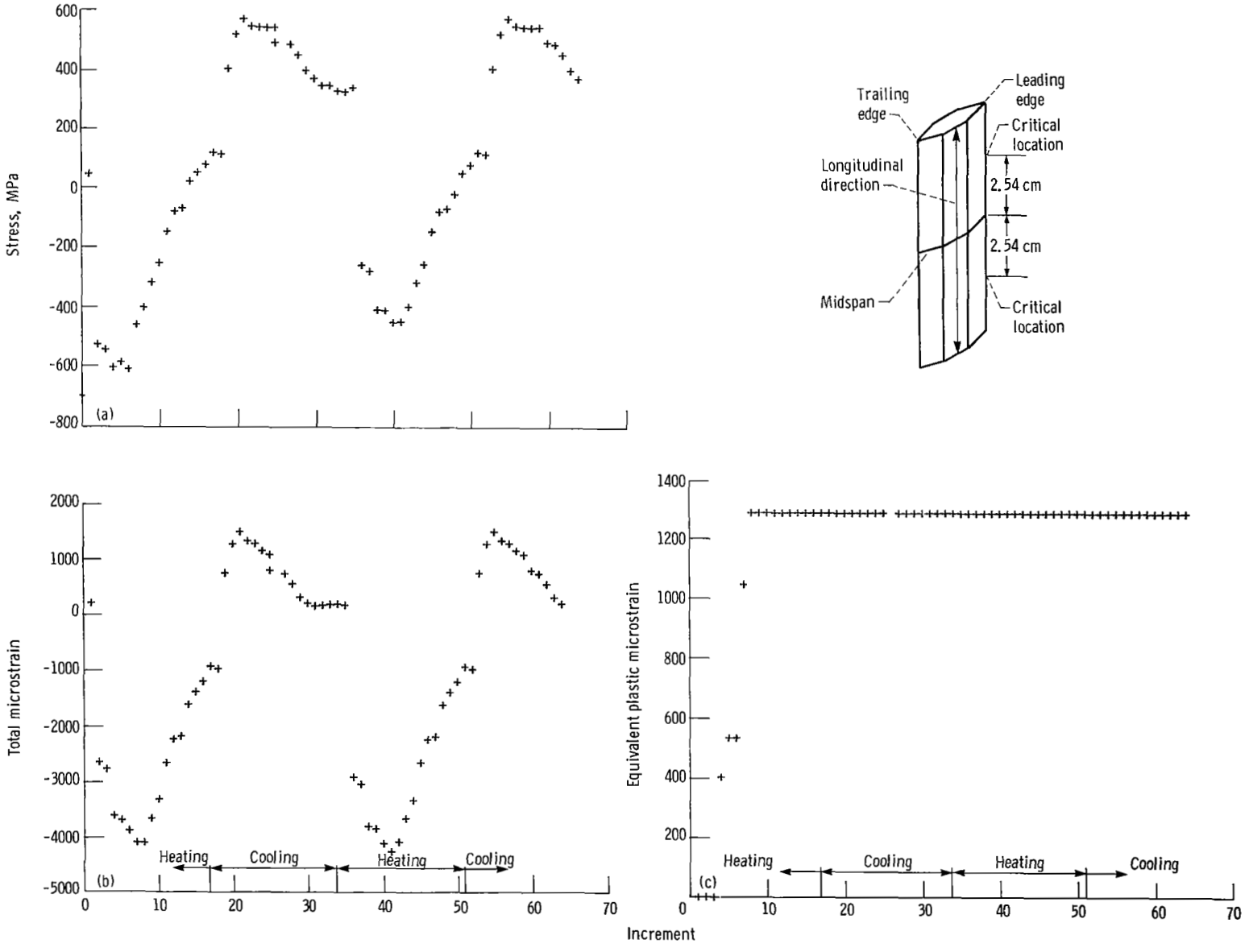

(a) Stress. (b) Total strain. (c) Plastic strain.

Figure 7. - Combined model analysis results (at critical location).

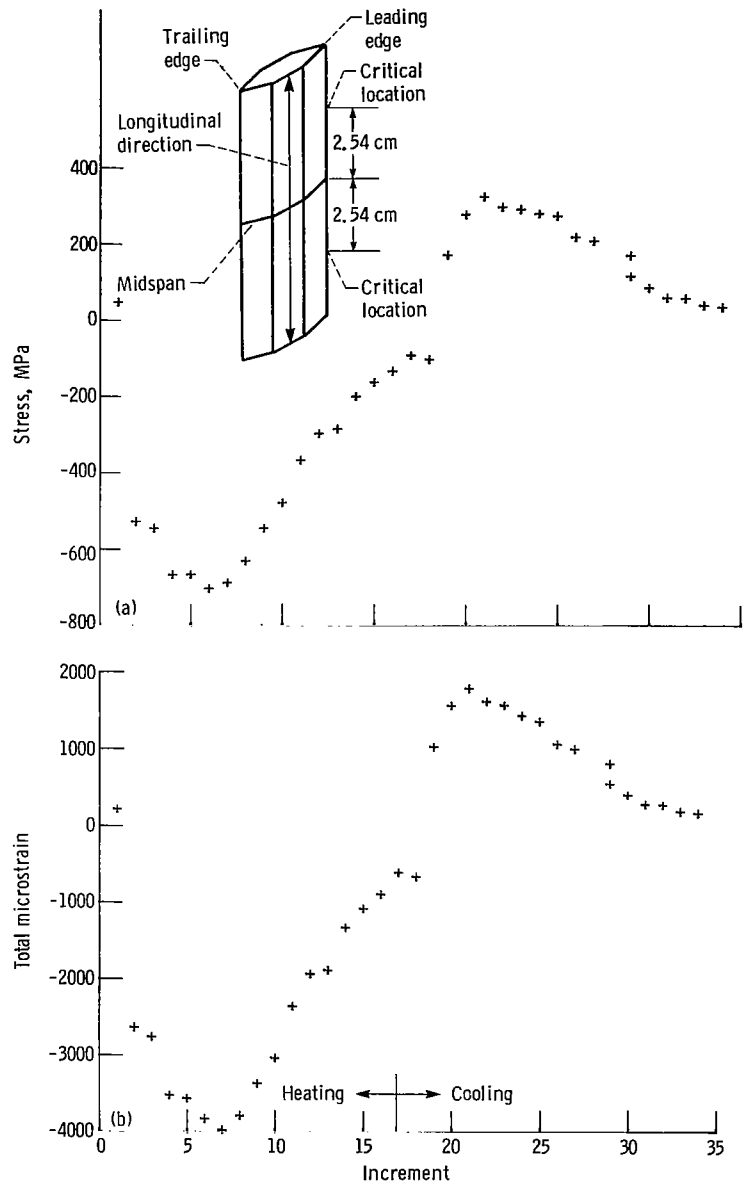

(a) Stress.
(b) Total strain.

Figure 6. - Elastic analysis results (at critical location).

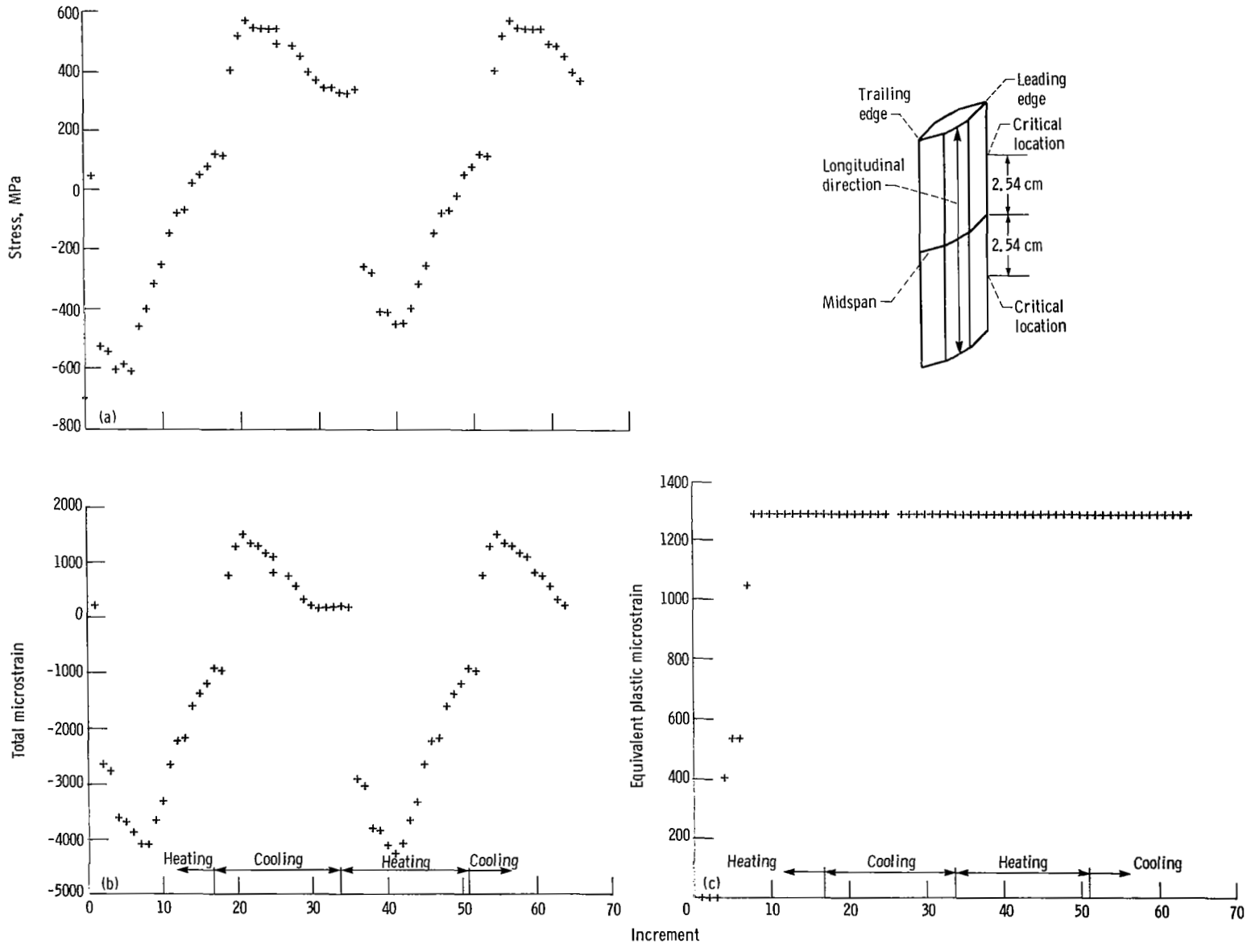

(a) Stress. (b) Total strain. (c) Plastic strain.

Figure 7. - Combined model analysis results (at critical location).

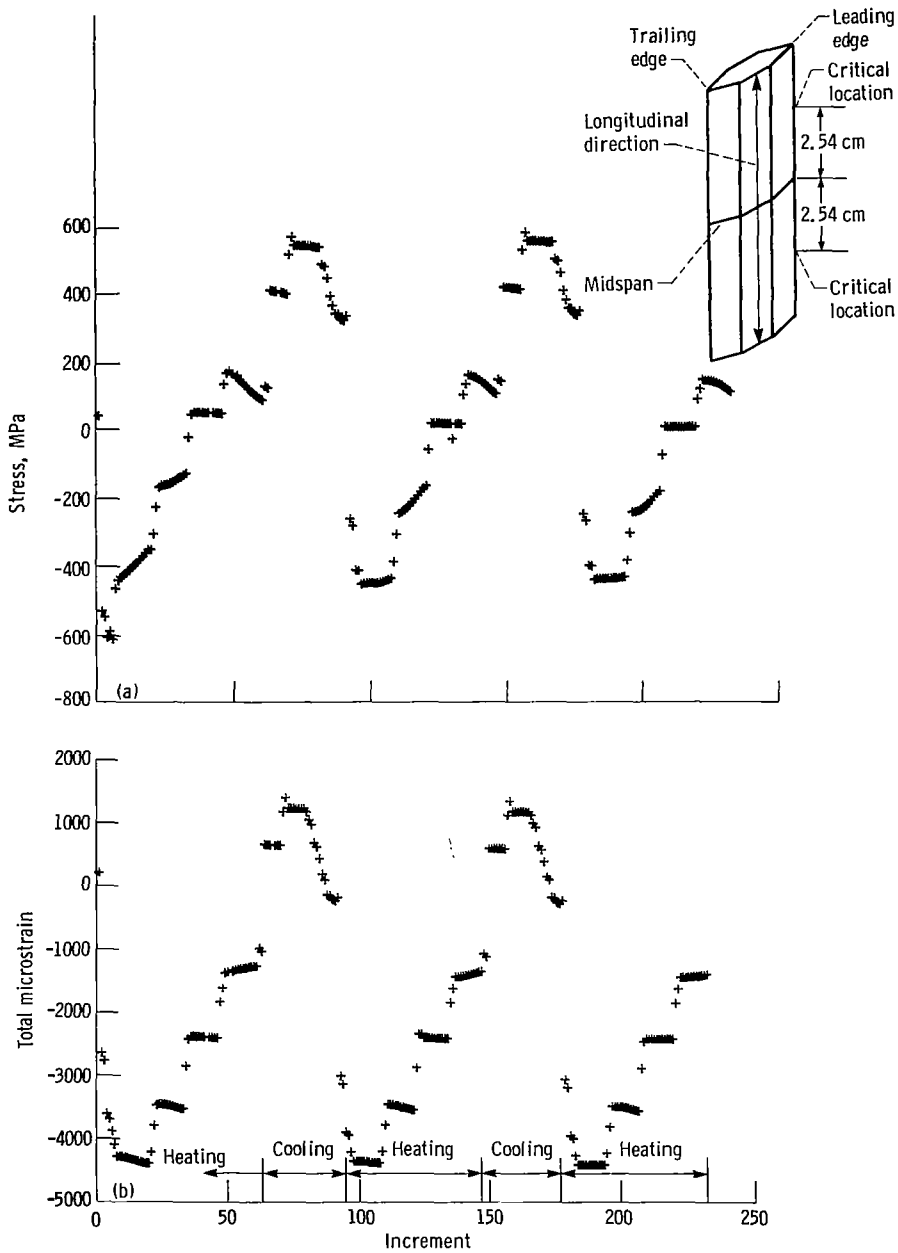

(a) Stress.
(b) Total strain.

Figure 8. - Combined-creep model analysis results (at critical location).

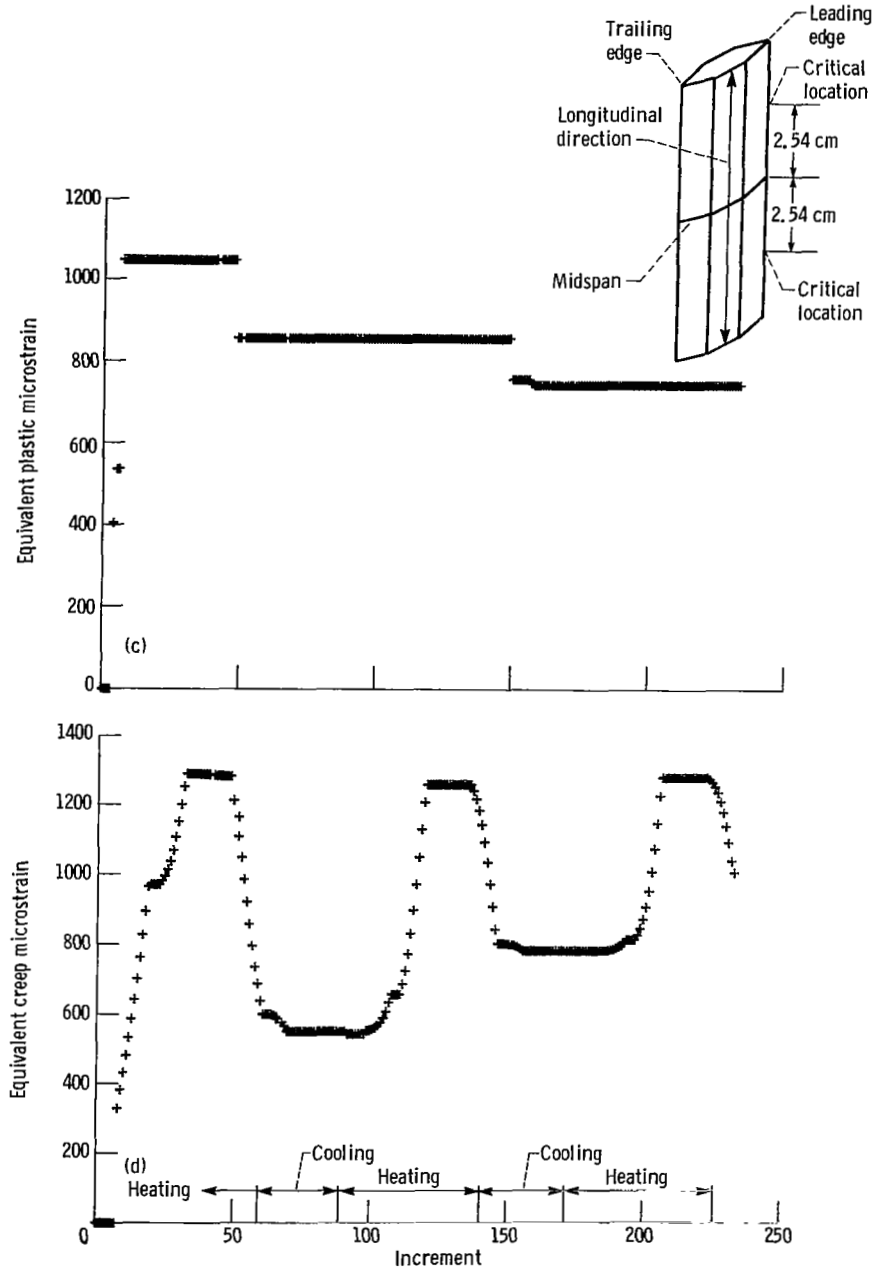

(c) Plastic strain.
(d) Creep strain.

Figure 8. - Concluded.

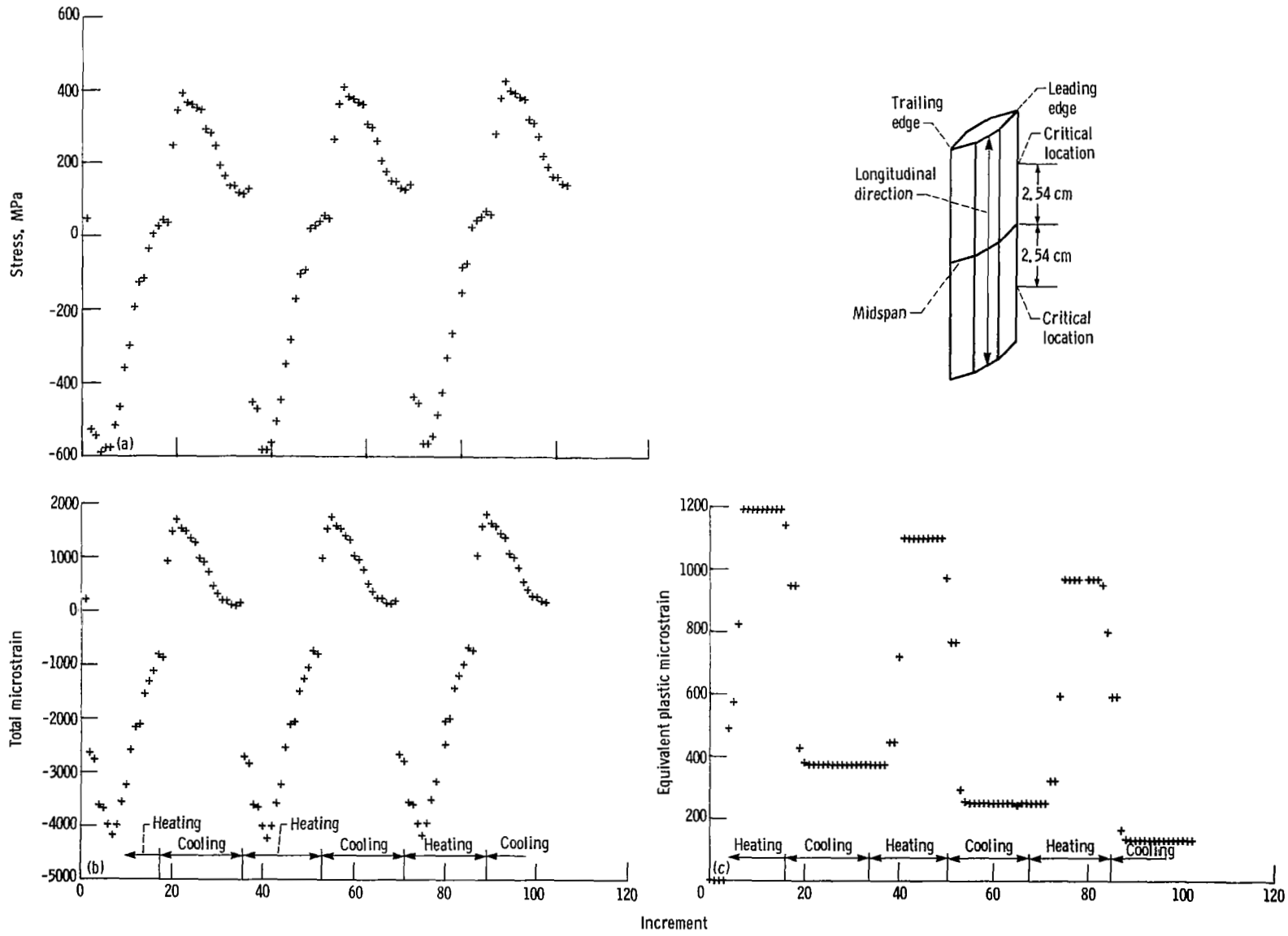

(a) Strain. (b) Total strain. (c) Plastic strain.

Figure 9. - Kinematic model analysis results (at critical location).

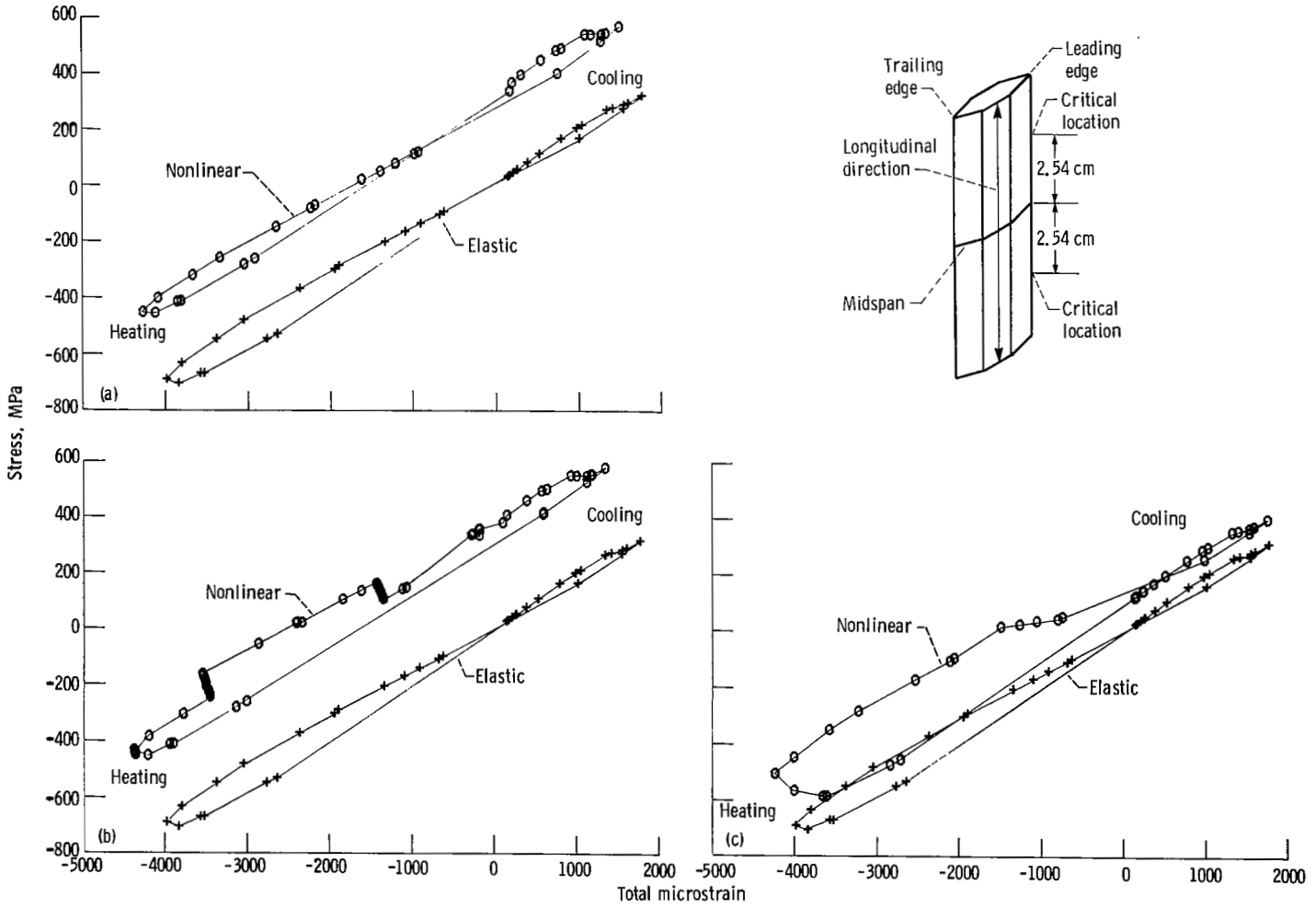

(a) Combined isotropic-kinematic hardening.
(b) Combined isotropic-kinematic hardening with creep.
(c) Kinematic hardening.

Figure 10. - Effect of nonlinear constitutive model on stress-strain response (second cycle, at critical location).

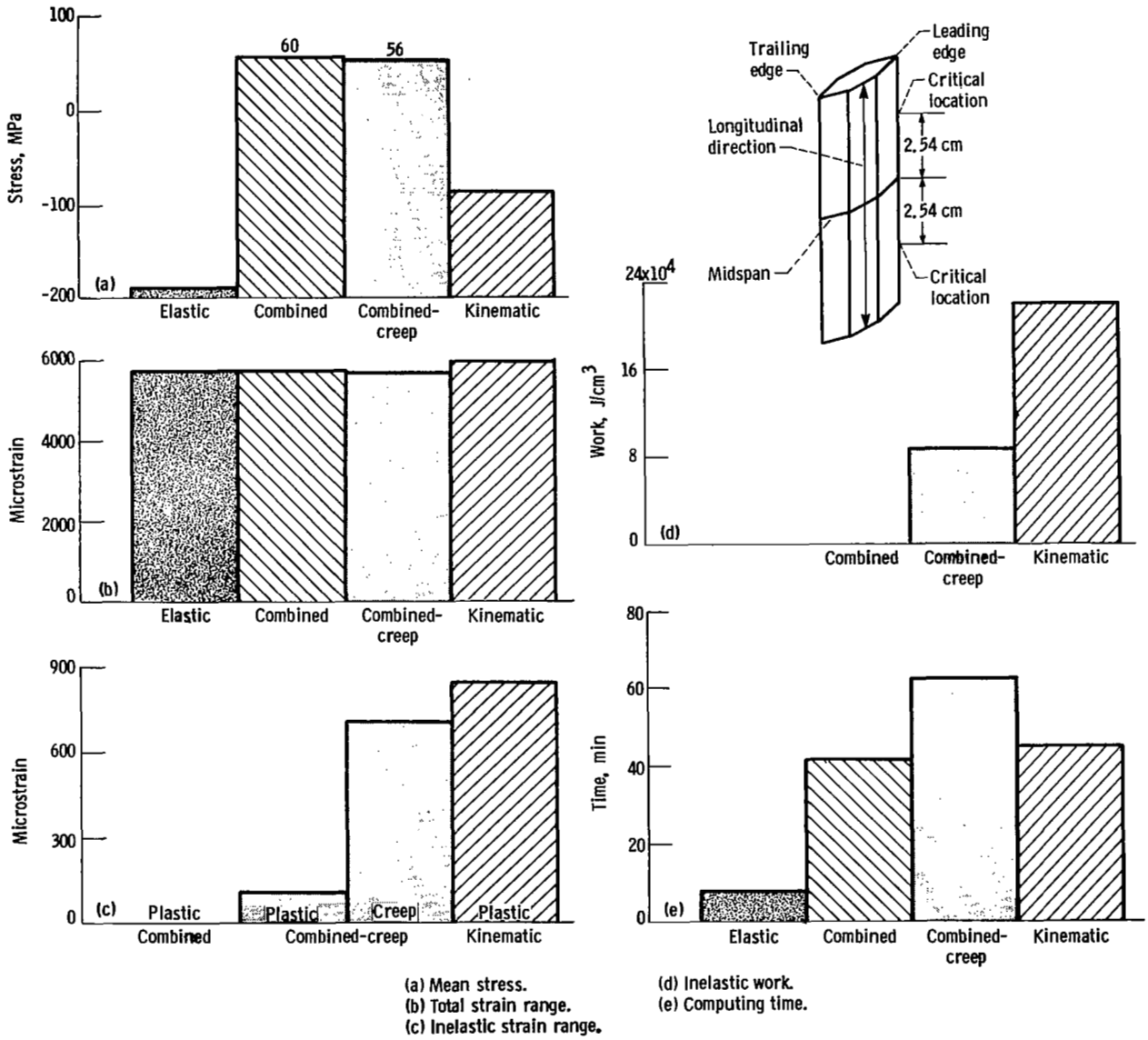

(a) Mean stress.
(b) Total strain range.
(c) Inelastic strain range.
(d) Inelastic work.
(e) Computing time.

Figure 11. - Effect of stress-strain behavior on cycle parameters (second cycle, at critical location).

Contour	Temperature, °C
1	604
2	644
3	684
4	725
5	765
6	805
7	846
8	886
9	926
10	966

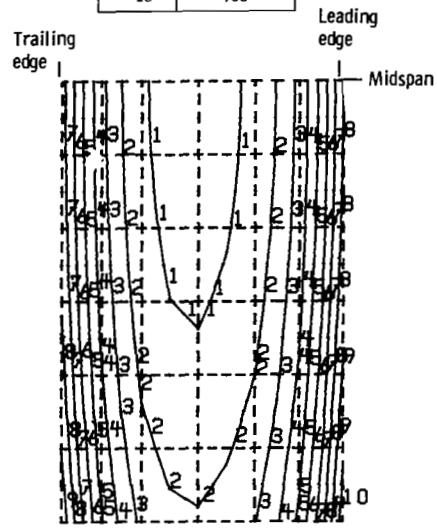

(a) Temperature.

Figure 12. - Temperature-stress-strain distributions along midchord plane after 30 seconds of heating (second cycle, at critical location).

Contour	Stress, MPa			
	Elastic	Combined	Combined-creep	Kinematic
1	69	60	57	65
2	142	107	105	115
3	215	153	153	166
4	288	199	201	216
5	361	246	249	267
6	434	292	296	318
7	507	339	345	368
8	581	385	392	419
9	654	432	441	470
10	724	478	488	520

Contour	Stress, MPa			
	Elastic	Combined	Combined-creep	Kinematic
1	-758	-511	-504	-543
2	-661	-441	-435	-470
3	-564	-372	-365	-398
4	-468	-302	-296	-325
5	-372	-232	-227	-252
6	-276	-163	-157	-179
7	-179	-93	-88	-106
8	-83	-23	-18	-33
9	13	46	51	39
10	110	116	121	112

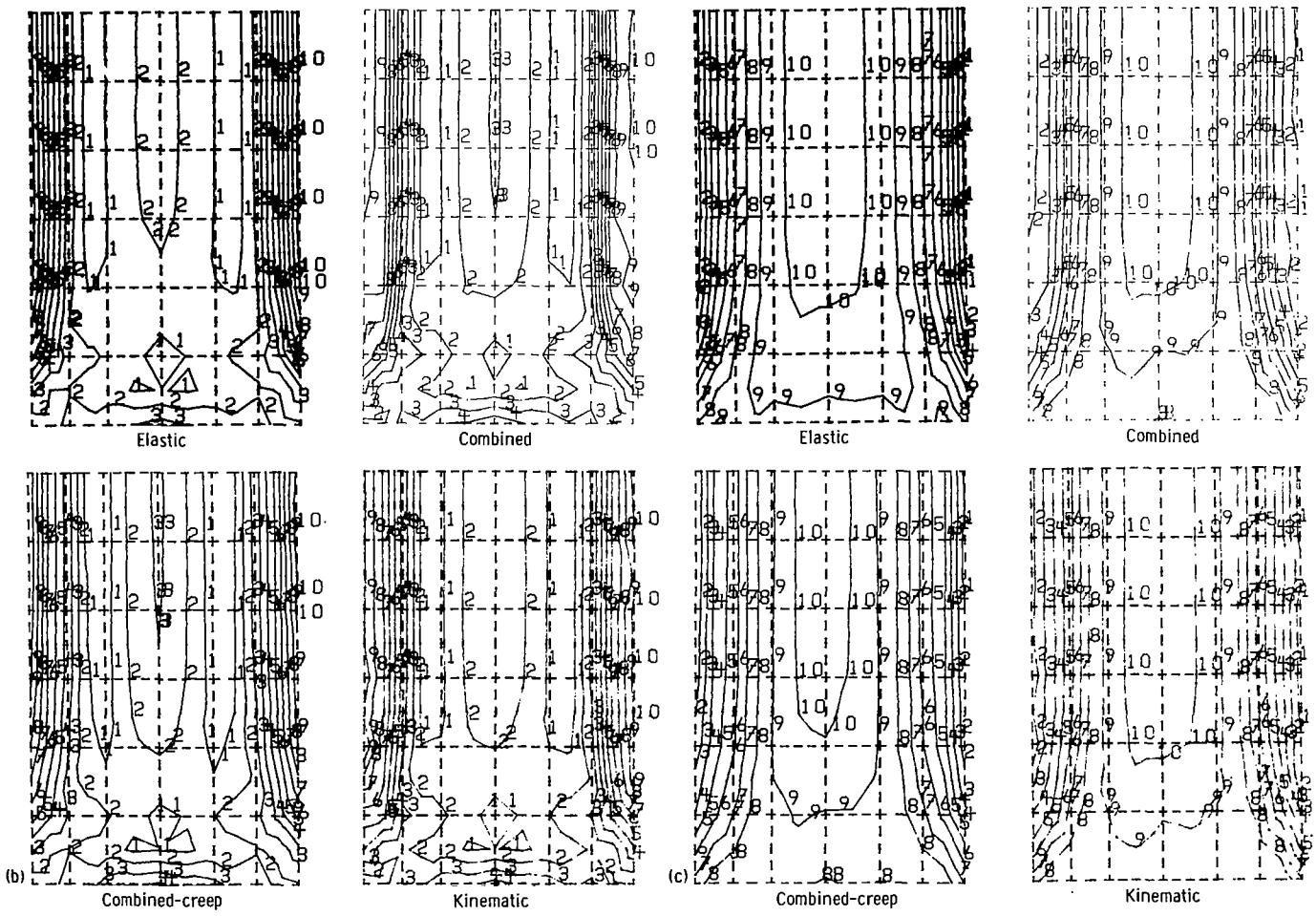

(b) Effective stress. (c) Longitudinal stress.

Figure 12. - Continued.

Contour	Microstrain			
	Elastic	Combined	Combined-creep	Kinematic
1	380	410	430	430
2	810	870	910	880
3	1240	1330	1380	1330
4	1660	1790	1860	1790
5	2090	2250	2330	2240
6	2520	2710	2810	2690
7	2950	3170	3280	3150
8	3380	3630	3760	3600
9	3810	4090	4230	4050
10	4240	4550	4710	4510

Contour	Microstrain			
	Combined, plastic	Combined-creep		Kinematic, plastic
		Plastic	Creep	
1	90	90	70	40
2	280	270	200	190
3	460	460	330	340
4	650	640	470	480
5	840	820	600	630
6	1020	1000	740	770
7	1210	1190	870	920
8	1390	1370	1000	1060
9	1580	1550	1140	1210
10	1760	1730	1270	1350

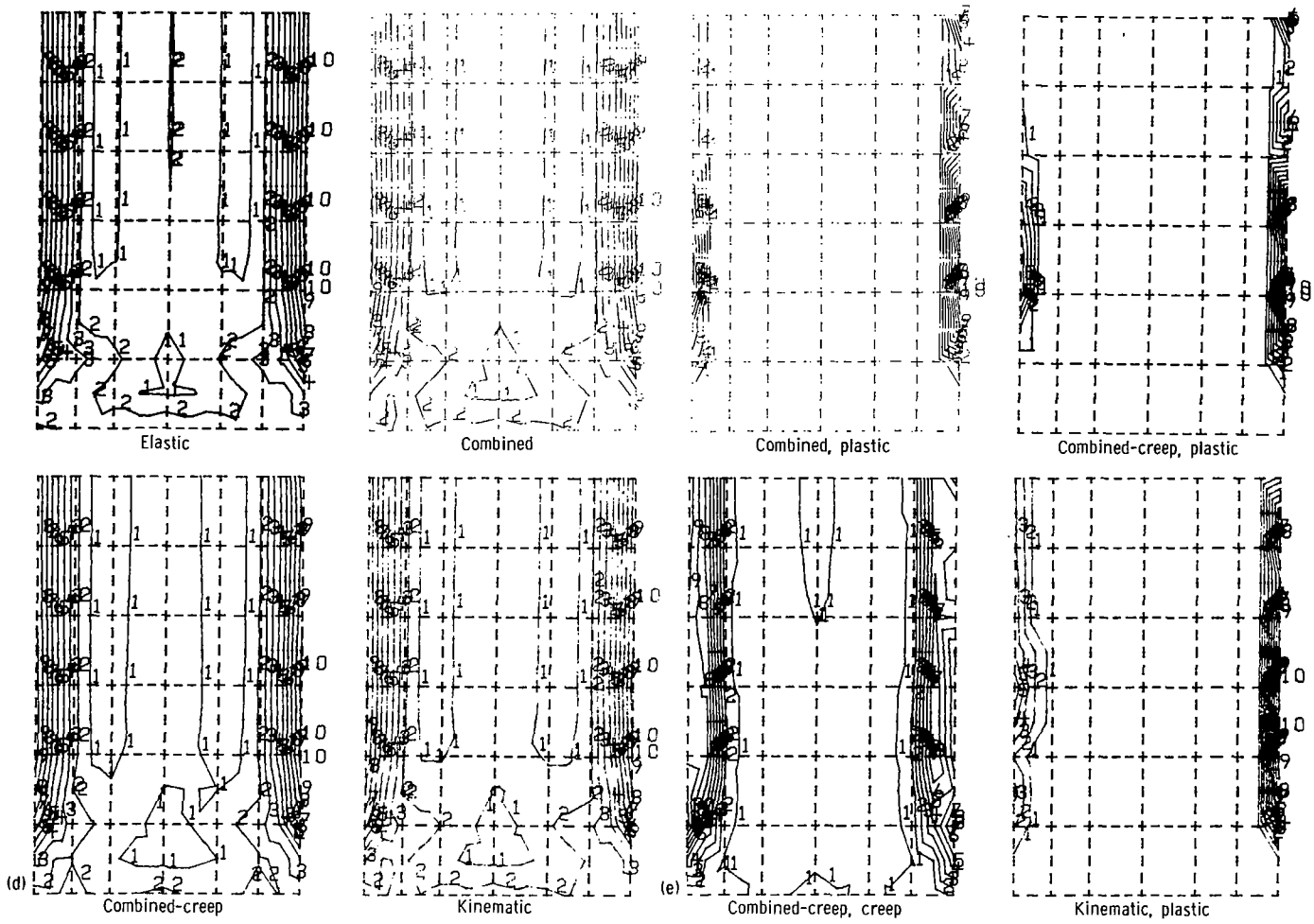

(d) Equivalent total strain.

(e) Equivalent inelastic strain.

Figure 12. - Concluded.

Contour	Temperature, ^{o}C
1	754
2	778
3	801
4	825
5	848
6	871
7	894
8	917
9	941
10	965

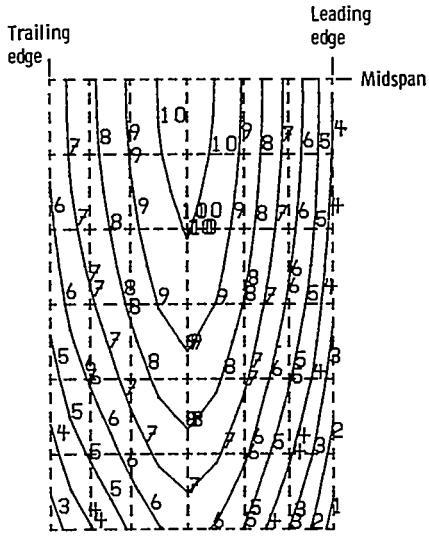

(a) Temperature.

Figure 13. - Temperature-stress-strain distributions along midchord plane after 9 seconds of cooling (second cycle, at critical location).

Contour	Stress, MPa			
	Elastic	Combined	Combined-creep	Kinematic
1	21	38	51	33
2	58	104	115	89
3	95	170	179	145
4	132	236	243	201
5	169	303	307	256
6	206	369	371	312
7	243	436	434	368
8	280	502	498	424
9	317	568	562	480
10	354	634	626	536

Contour	Stress, MPa			
	Elastic	Combined	Combined-creep	Kinematic
1	-115	-107	-108	-112
2	-63	-24	-25	-37
3	-10	59	59	38
4	42	142	142	114
5	95	225	225	189
6	148	308	309	264
7	201	390	392	339
8	253	473	476	414
9	306	556	559	490
10	359	639	643	565

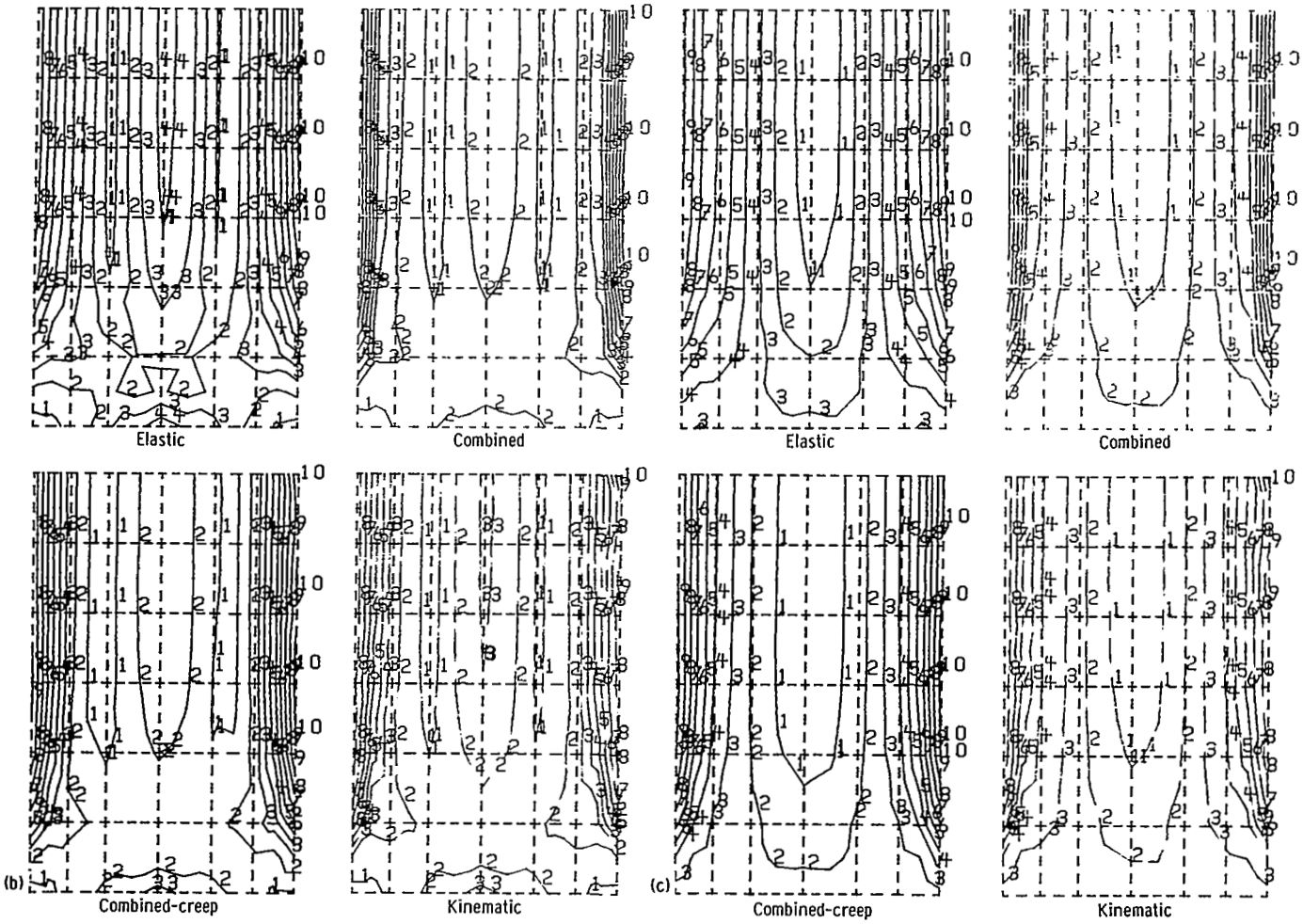

(b) Effective stress. (c) Longitudinal stress.

Figure 13. - Continued.

Contour	Microstrain			
	Elastic	Combined	Combined-creep	Kinematic
1	130	130	90	140
2	330	330	280	360
3	530	530	470	570
4	740	730	650	780
5	940	930	840	1000
6	1150	1130	1030	1210
7	1350	1330	1220	1430
8	1560	1530	1410	1640
9	1760	1730	1600	1860
10	1960	1930	1790	2070

Contour	Microstrain			
	Combined, plastic	Combined-creep		Kinematic, plastic
		Plastic	Creep	
1	80	90	90	30
2	270	270	290	140
3	460	460	500	260
4	650	640	700	380
5	830	820	900	490
6	1020	1000	1110	610
7	1200	1190	1310	720
8	1390	1370	1510	840
9	1580	1550	1710	950
10	1760	1730	1920	1070

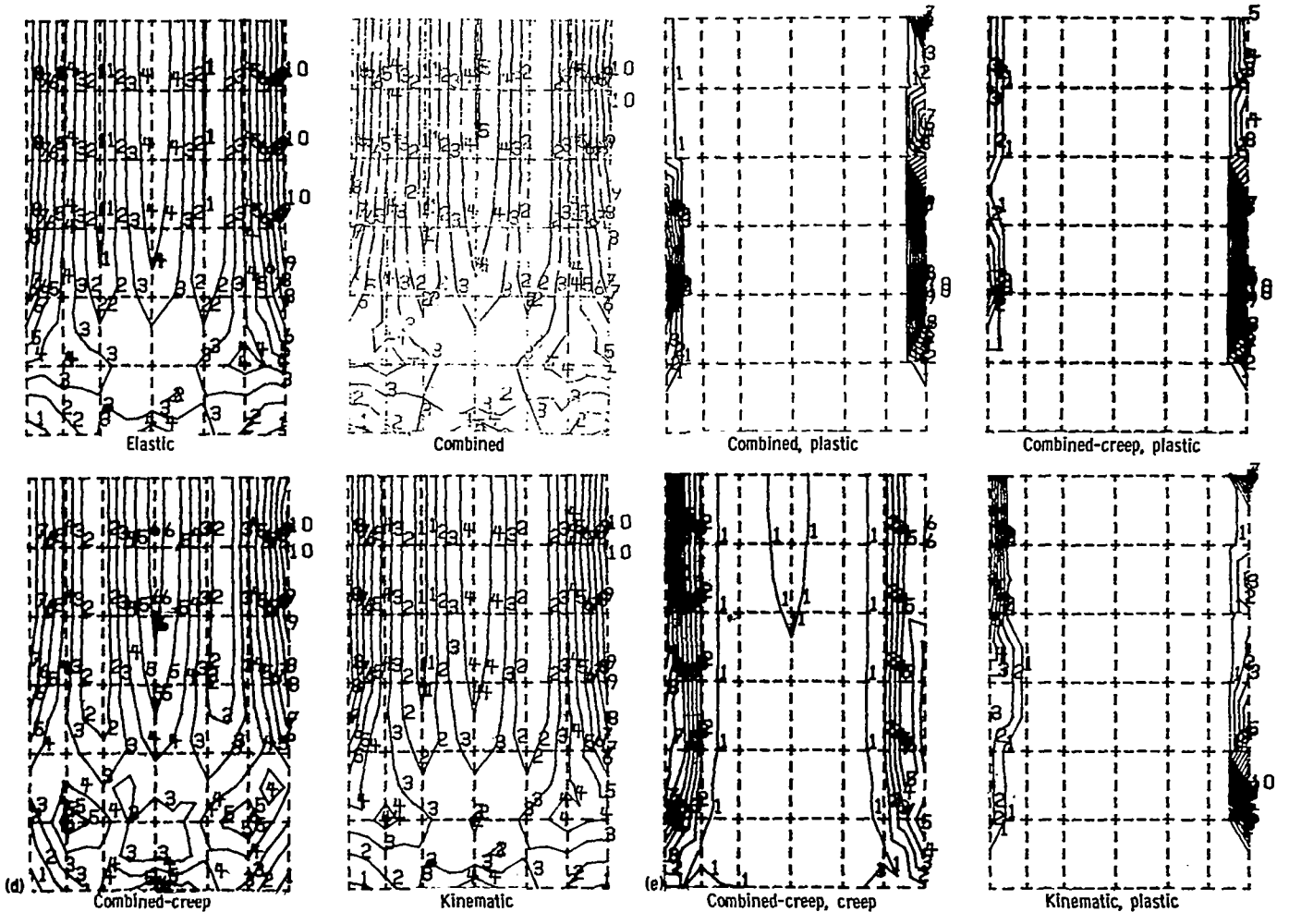

(d) Equivalent total strain. (e) Equivalent inelastic strain.

Figure 13. - Concluded.

1. Report No.	2. Government Accession No.	3. Recipient's Catalog No.
NASA TP-2055		

4. Title and Subtitle	5. Report Date
MATERIALS CONSTITUTIVE MODELS FOR NONLINEAR ANALYSIS OF THERMALLY CYCLED STRUCTURES	OCTOBER 1982
	6. Performing Organization Code: 505-33-22
7. Author(s): Albert Kaufman and Larry E. Hunt	8. Performing Organization Report No.: E-1125
	10. Work Unit No.
9. Performing Organization Name and Address: National Aeronautics and Space Administration, Lewis Research Center, Cleveland, Ohio 44135	11. Contract or Grant No.
	13. Type of Report and Period Covered: Technical Paper
12. Sponsoring Agency Name and Address: National Aeronautics and Space Administration, Washington, D.C. 20546	14. Sponsoring Agency Code

15. Supplementary Notes

Albert Kaufman, Lewis Research Center; Larry E. Hunt, University of Arizona, Tucson, Ariz. (work done at Lewis Research Center under NASA Grant NAG3-45).

16. Abstract

Effects of inelastic materials models on computed stress-strain solutions for thermally loaded structures were studied by performing nonlinear (elastoplastic creep) and elastic structural analyses on a prismatic, double-edge wedge specimen of IN 100 alloy that had been subjected to thermal cycling in fluidized beds. Four incremental plasticity-creep models (isotropic, kinematic, combined isotropic-kinematic, and combined plus transient creep) were exercised for the problem by using the MARC nonlinear, finite-element computer program. Maximum total strain ranges computed from the elastic and nonlinear analyses agreed within 5 percent. Mean cyclic stresses, inelastic strain ranges, and inelastic work were significantly affected by the choice of inelastic constitutive model. The computing time per cycle for the nonlinear analyses was more than five times that required for the elastic analysis.

17. Key Words (Suggested by Author(s))	18. Distribution Statement
Nonlinear structural analysis Thermal fatigue	Unclassified - unlimited STAR Category 39

19. Security Classif. (of this report)	20. Security Classif. (of this page)	21. No. of Pages	22. Price*
Unclassified	Unclassified	25	A02

* For sale by the National Technical Information Service, Springfield, Virginia 22161 NASA-Langley, 1982

3 1 1U,D, 821013 S00903DS
DEPT OF THE AIR FORCE
AF WEAPONS LABORATORY
ATTN: TECHNICAL LIBRARY (SUL)
KIRTLAND AFB NM 87117